RESEARCH ARTICLE

Check for updates

First series of mixed (P^{III}, Se^{IV})-heteroatomoriented rare-earth-embedded polyoxotungstates containing distinct building blocks†

Lulu Liu, Jun Jiang, Xiaoyi Liu, Guoping Liu, Dan Wang, Lijuan Chen* and Junwei Zhao 🆔 *

By a self-assembly reaction strategy accompanying the step-by-step introduction of simple reactants, a series of unprecedented mixed-heteroatom-oriented rare-earth-embedded heteropolyoxotungstates $[H_2N(CH_3)_2]_{12}Na_2[RE_2(H_2O)_7(W_4O_9)(HPSeW_{15}O_{54})\ (SeW_9O_{33})_2]\cdot 44H_2O$ (RE = Ce^{3+} (**1**), Pr^{3+} (**2**), Nd^{3+} (**3**), Sm^{3+} (**4**), Gd^{3+} (**5**), Tb^{3+} (**6**), Ho^{3+} (**7**), Er^{3+} (**8**)) were successfully achieved. It is worth highlighting that their polyoxoanions were synergistically established by two trivacant Keggin Se^{IV}-inserted $[B-\alpha-SeW_9O_{33}]^{8-}$ clusters and one trivacant Dawson P^{III}-and-Se^{IV}-inserted $[HPSeW_{15}O_{54}]^{10-}$ segment. Significantly, $[HPSeW_{15}O_{54}]^{10-}$ is a rarely reported polyoxometalate (POM) unit and can be viewed as a new member derived from one plenary Dawson P^{III}-and-Se^{IV}-inserted polyoxoanion by removing three {WO$_6$} octahedra in the polar position. Moreover, the composite of **1** and carboxyl-functionalized multi-walled carbon nanotubes (CMWCNTs) was modified onto a glass carbon electrode (GCE) to construct the **1**@CMWCNT-GCE electrochemical sensor (ECS). In PBS buffer (pH 7.00), we investigated the electrochemical sensing properties of **1**@CMWCNT-GCE ECS toward simultaneously detecting dopamine (DA) and uric acid (UA). The **1**@CMWCNT-GCE ECS exhibited good sensing performances toward DA and UA with a low detection limit (1.61 μmol L^{-1} for DA and 5.41 μmol L^{-1} for UA) and high stability. This work not only shows that the synergistic interaction of diverse heteroatoms (Has) can facilitate creating captivating structures of POMs, but also promotes the applications of POM-based materials in recognizing bioactive molecules.

Henan Key Laboratory of Polyoxometalate Chemistry, College of Chemistry and Chemical Engineering, Henan University, Kaifeng, Henan 475004, China.
E-mail: ljchen@henu.edu.cn, zhaojunwei@henu.edu.cn

†Electronic supplementary information (ESI) available: Synthetic methods, related structural figures, IR spectra and TG curves of **1–8**. CCDC 2023680–2023685, 2033453 and 2033454. For ESI and crystallographic data in CIF or other electronic format see DOI: 10.1039/d0qi01031f

Introduction

Being formed by the polymerization of early transition-metal elements in a high oxidation state through bridging oxygen atoms, polyoxometalates (POMs) are considered as a promising subclass of polynuclear metal-oxo clusters and have displayed fascinating structural features and various applications in catalysis, optics, medicine, magnetism, and nanotechnology.[1–7] According to the case whether heteroatoms (HAs) (for example, Sb^{III}, Se^{IV}, Si^{IV}, P^{V}) are included or not in the structures, POMs can be divided into isopolyoxometalates (IPOMs) and heteropolyoxometalates (HPOMs). It has been abundantly proved that HPOMs manifest better structural stability and

more wide-ranging application potentials than IPOMs.[8–12] Especially, compared with those featuring the tetrahedral geometry of XO$_4$ (X = Ge^{IV}, Si^{IV}, P^{V}, As^{V}, *etc.*), HAs bearing lone electron pairs and the trigonal pyramidal geometry of XO$_3$ (X = Sb^{III}, Bi^{III}, As^{III}, Se^{IV}, Te^{IV}, *etc.*) show better convenience and availability in the construction of lacunary or open POM building units with more reactive sites,[13,14] because the spatial stereoscopic effect of the lone electron pairs on the XO$_3$ groups can effectively prevent the formation of plenary structures.[15,16]

In comparison with the group-valence HA-inserted (such as Ge^{IV}, Si^{IV}, P^{V}, As^{V}) HPOM fragments, substitution of the subgroup-valence HAs (such as P^{III}, Sb^{III}, Bi^{III}, As^{III}, Se^{IV}, Te^{IV}) for the group-valence HAs can increase the negative charge of the resulting HPOM fragments, which is favorable for the incorporation of extraneous metal ions into the HPOM skeletons.[17,18] Thus, introducing subgroup-valence HAs into HPOMs can provide more opportunities for developing novel HPOM derivatives with fabulous structures and unexpected performances. In addition, since the first rare-earth (RE)-containing POM (RECPOM) $[H_6CeMo_{12}O_{42}]^{2-}$ was discovered in 1914 by Barbieri,[19] which was considered as a milestone

achievement in RECPOM chemistry, RECPOMs have aroused more and more interest. It has been demonstrated that RE ions have great potential to construct innovative RECPOMs because of their larger ion radii, flexible coordination styles, and outstanding oxyphilicity.[20–25] Therefore, RE-containing HPOMs (RECHPOMs) have long been investigated owing to the synergistic effect of the RE ions and the sub-group-valence HAs in the reaction process.[26] In 1997, the best-known multi-As^{III}-and-Ce^{III}-encapsulated cyclic RECHPOM cluster [As$_{12}$Ce$_{16}$(H$_2$O)$_{36}$W$_{148}$O$_{524}$]$^{76–}$ was first isolated by Pope's group (Fig. 1a).[27] In 2009, Patzke et al. discovered the longest Gd^{III}-inserted arsenotungstate (AT) [Gd$_8$As$_{12}$W$_{124}$O$_{432}$(H$_2$O)$_{22}$]$^{60–}$ consisting of twelve [AsW$_9$O$_{33}$]$^{9–}$ segments (Fig. 1b).[28] The infrequent multi-RE included seleno-tungstate (ST) and tellurotungstate (TT) aggregates [{(XO$_3$)W$_{10}$O$_{34}$}$_8${(Ce$_8$H$_2$O)$_{20}$}(WO$_2$)$_4$(W$_4$O$_{12}$)]$^{48–}$ (X = Se^{IV}, Te^{IV}; Fig. 1c) and [{(SeO$_3$)W$_{10}$O$_{34}$}$_8${Ce$_8$(H$_2$O)$_{20}$}(WO$_2$)$_4${(W$_4$O$_6$)Ce$_4$(H$_2$O)$_{14}$(SeO$_3$)$_4$(NO$_3$)$_2$}]$^{34–}$ (Fig. 1d) were addressed by Su and collaborators in 2013.[29] A class of scarce 3d–4f heterometallic tungstoantimonates (TAs) [RE$_3$(H$_2$O)$_5$Ni^{II}(H$_2$O)$_3$(Sb$_4$O$_4$)(SbW$_9$O$_{33}$)$_3$(Ni^{II}W$_6$O$_{24}$)(WO$_2$)$_3$(CH$_3$COO)]$^{16–}$ (RE = La^{3+}, Pr^{3+}, Nd^{3+}) were later reported by Kong and co-workers in 2017, which were built by a central {NiW$_6$} segment and three RE-connecting {SbW$_9$} clusters (Fig. 1e).[30] Creatively, in 2018, our group communicated a giant cerium–bismuth tungstate nanocluster {[W$_{14}$Ce$_6^{IV}$O$_{61}$]([W$_3$Bi$_6$Ce$_3^{III}$(H$_2$O)$_3$O$_{14}$][B-α-BiW$_9$O$_{33}$]$_3$)$_2$}$^{34–}$ featuring 104 metal centers (Fig. 1f).[15]

It can be readily found that the majority of reported RECHPOMs only contain one type of HA in their structures. In the past several years, we have obtained some RECHPOMs consisting of one type of HA.[17,18,20–25] However, related investigations on RECHPOMs including two types of HAs are greatly

underdeveloped hitherto, and still represent an exceedingly fascinating and extremely challenging topic. Under this background, we launched systematic explorations on RECHPOMs including two types of HAs based on the following considerations: (a) according to previous research results, the SeO$_3^{2–}$ ion with lone-pair electrons and three binding oxygen atoms exhibits a trigonal pyramidal geometry and tends to form highly active lacunary ST building units in the W–Se–O system,[29] and then these resulting lacunary ST segments can readily combine with RE ions to build novel and large RECHPOMs;[31,32] (b) the phosphite anion ([HPO$_3$]$^{2–}$) with a binding proton and three oxygen atoms presents an approximately tetrahedral fashion, which allows it to behave with high reactivity to easily integrate with tungsten-oxo cluster fragments to generate lacunary phosphotungstate building units;[33,34] (c) if SeO$_3^{2–}$ and H$_3$PO$_3$ can be simultaneously introduced into the tungstate and RE system, sophisticatedly controlling the proper reaction conditions should result in novel RECHPOMs including two types of HAs, in which trigonal pyramidal [SeO$_3$]$^{2–}$ and tetrahedral [HPO$_3$]$^{2–}$ groups play a directing role in the synthesis procedure. Moreover, the coexistence of trigonal pyramidal [SeO$_3$]$^{2–}$ and tetrahedral [HPO$_3$]$^{2–}$ groups in the reaction system may also provide a great possibility to generate the novel phenomenon that an infrequent HPOM fragment consists of two types of HAs, which will greatly enrich the structural types of HPOM fragments and promote the development of POM chemistry. Thus, we prepared a series of unprecedented mixed P^{III} and Se^{IV} heteroatom-oriented RE-embedded HPOTs [H$_2$N(CH$_3$)$_2$]$_{12}$Na$_2$[RE$_2$(H$_2$O)$_7$(W$_4$O$_9$)(HPSeW$_{15}$O$_{54}$)(SeW$_9$O$_{33}$)$_2$]·44H$_2$O [RE = Ce^{3+} (1), Pr^{3+} (2), Nd^{3+} (3), Sm^{3+} (4), Gd^{3+} (5), Tb^{3+} (6), Ho^{3+} (7), Er^{3+} (8)] by a self-assembly reaction strategy accompanying the step-by-step introduction of simple commercial reactants
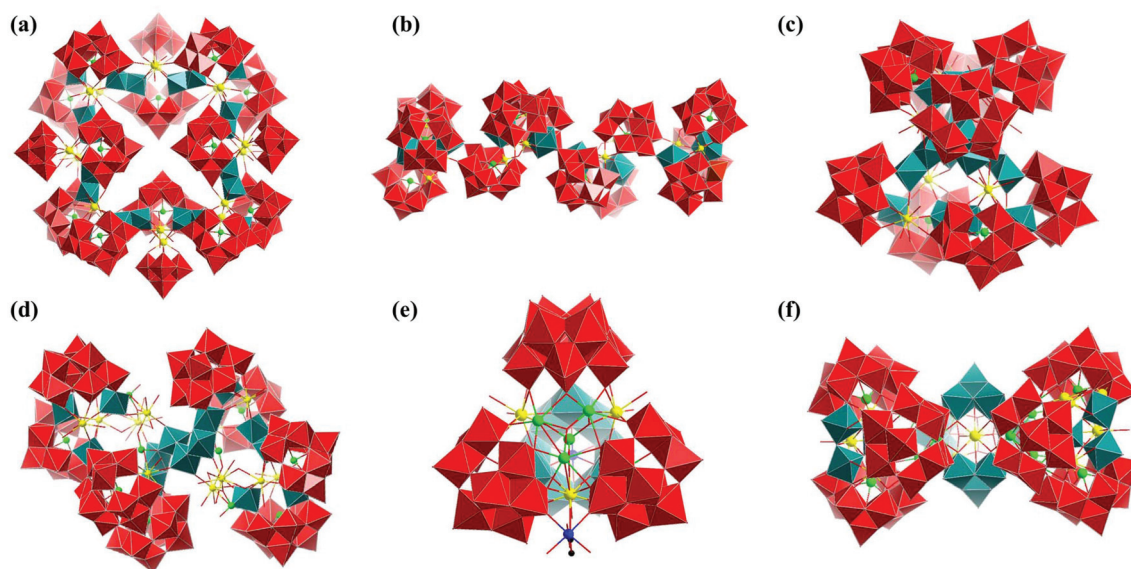

Fig. 1 Some typical RECHPOMs: (a) [As$_{12}$Ce$_{16}$(H$_2$O)$_{36}$W$_{148}$O$_{524}$]$^{76–}$, (b) [Gd$_8$As$_{12}$W$_{124}$O$_{432}$(H$_2$O)$_{22}$]$^{60–}$, (c) [{(XO$_3$)W$_{10}$O$_{34}$}$_8${(Ce$_8$H$_2$O)$_{20}$}(WO$_2$)$_4$(W$_4$O$_{12}$)]$^{48–}$, (d) [{(SeO$_3$)W$_{10}$O$_{34}$}$_8${Ce$_8$(H$_2$O)$_{20}$}(WO$_2$)$_4${(W$_4$O$_6$)Ce$_4$(H$_2$O)$_{14}$(SeO$_3$)$_4$(NO$_3$)$_2$}]$^{34–}$, (e) [RE$_3$(H$_2$O)$_5$Ni^{II}(H$_2$O)$_3$(Sb$_4$O$_4$)(SbW$_9$O$_{33}$)$_3$(Ni^{II}W$_6$O$_{24}$)(WO$_2$)$_3$(CH$_3$COO)]$^{16–}$, (f) {[W$_{14}$CeIV$_6$O$_{61}$]([W$_3$Bi$_6$Ce^{III}$_3$(H$_2$O)$_3$O$_{14}$][B-α-BiW$_9$O$_{33}$]$_3$)$_2$}$^{34–}$.

This journal is © the Partner Organisations 2020

Inorg. Chem. Front., 2020, **7**, 4640–4651 | **4641**

(Fig. S1†). The most interesting characteristic was that the trimeric $[RE_2(H_2O)_7(W_4O_9)(HPSe\ W_{15}O_{54})(SeW_9O_{33})_2]^{14-}$ polyoxoanion (POA) in **1–8** was constituted by two trivacant Keggin $[B-\alpha-SeW_9O_{33}]^{8-}$ segments and one trivacant Dawson $[HPSeW_{15}O_{54}]^{10-}$ segment linked by a hexanuclear $[Ce_2(H_2O)(W_4O_9)]^{12+}$ heterometallic cluster. It should be emphasized that the trivacant $[HPSeW_{15}O_{54}]^{10-}$ segment is a new member derived from one plenary Dawson P^{III}-and-Se^{IV}-inserted POA by removing three $\{WO_6\}$ octahedra in the polar positions and is a rarely seen HPOT fragment in POM field. Furthermore, **1** was composited with carboxyl-functionalized multi-walled carbon nanotubes (CMWCNTs) to form the **1**@CMWCNT complex, which was used to modify a glass carbon electrode (GCE) to construct the **1**@CMWCNT-GCE electrochemical sensor (ECS). The experimental results indicated that the obtained **1**@CMWCNT-GCE ECS showed great potential to synchronously detect dopamine (DA) and uric acid (UA) in a NaH_2PO_4–Na_2HPO_4 phosphate buffer solution (PBS, pH 7.00).

Results and discussion

Synthesis

1–8 were successfully synthesized based on $Na_2WO_4 \cdot 2H_2O$, Na_2SeO_3, DMA·HCl (dimethylamine hydrochloride), H_3PO_3, and $RE(NO_3)_3 \cdot 6H_2O$ (RE = Ce^{3+}, Pr^{3+}, Nd^{3+}, Sm^{3+}, Gd^{3+}, Tb^{3+}, Ho^{3+}, Er^{3+}) as raw materials. RE ions were introduced into the system, forming unprecedented RECHPOMs **1–8** simultaneously consisting of two trivacant Keggin-type Se^{IV}-inserted $[B-\alpha-SeW_9O_{33}]^{8-}$ segments and one trivacant Dawson-type P^{III}-and-Se^{IV}-inserted $[HPSeW_{15}O_{54}]^{10-}$ segment. In order to

improve the reactivity of RE ions in this system, DMA·HCl was added as an organic solubilizer to promote the slow combination between RE cations and the *in situ*-generated HPOM fragments.[35] What's more, protonated $[HDMA]^+$ cations under acidic condition as organic counter-cations were beneficial to stabilize the resulting RECHPOM aggregates.[36,37] The pH value was also very crucial for the formation of the RECHPOMs. A lower pH environment of the reaction system could not only inhibit the slow hydrolysis of RE ions, but could also effectively enhance the synergistic reaction activity of Na_2SeO_3 and H_3PO_3 for inducing the integration of tungsten-oxo clusters, which provide good preconditions for the formation of RECHPOMs containing mixed-HA POM building blocks. In this study, **1–8** could be obtained in the pH range of 3.20–4.00, with pH 3.20 optimal and leading to high-quality crystals. The dosage of the reactants is another critical factor in the synthesis. The experimental results showed that the molar ratios of $n(Na_2WO_4 \cdot 2H_2O):n(Na_2SeO_3):n(DMA \cdot HCl):n(H_3PO_3):n(RE(NO_3)_3 \cdot 6H_2O)$ were 15.35 : 1.45 : 24.54 : 0.49 : 1.15–2.30. The larger the amount of RE^{3+} ions, the quicker the crystallization rate. Perfect quality crystals could be acquired when the final molar ratio of $n(Na_2WO_4 \cdot 2H_2O):n(RE(NO_3)_3 \cdot 6H_2O)$ was 15.35 : 1.61.

Structural description

The X-ray single-crystal diffraction results displayed that **1–8** are isomorphous and belong to the triclinic space group $P\bar{1}$. Besides, both the PXRD patterns (Fig. S2†) and IR spectra (Fig. S3†) also proved this result. So, we take **1** for example to specifically explain its crystal structure. The molecular structure of **1** consists of one unique trimeric **1a** POA (Fig. 2a), two
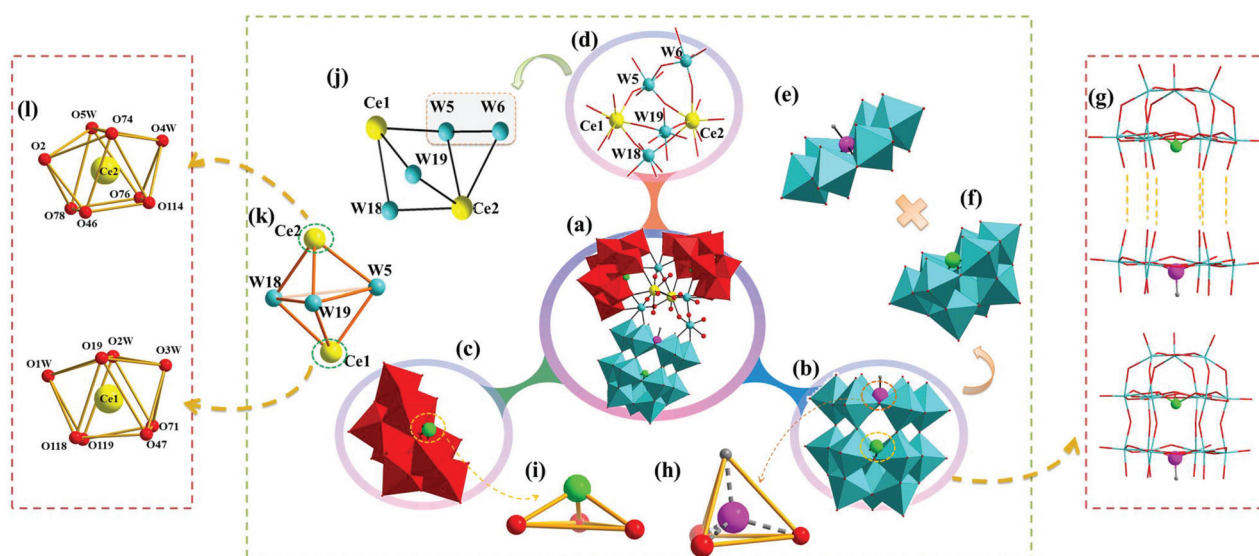

Fig. 2 (a) The **1a** POA. (b) The trivacant Dawson-type **1b** segment. (c) The trivacant Keggin $[B-\alpha-SeW_9O_{33}]^{8-}$ fragment. (d) View of the $[Ce_2(H_2O)(W_4O_9)]^{12+}$ cluster in **1a**. (e) The hypothetical hexavacant Keggin $[HPW_6O_{21}]^{2-}$ subunit in **1b**. (f) The trivacant Keggin $[B-\alpha-SeW_9O_{33}]^{8-}$ subunit in **1b**. (g) Connection motif between the $[B-\alpha-SeW_9O_{33}]^{8-}$ subunit and $[HPW_6O_{21}]^{2-}$ subunit in **1b**. (h) The tetrahedral geometry of the $\{HPO_3\}$ group in **1b**. (i) The trigonal pyramidal geometry of the $\{SeO_3\}$ group in **1b**. (j) The simplified connection mode of the $[Ce_2(H_2O)(W_4O_9)]^{12+}$ cluster. (k) Distorted trigonal bipyramid of $\{Ce_2W_3\}$. (l) The coordination geometry of $Ce1^{3+}$ and $Ce2^{3+}$ ions. (W: Red and turquoise octahedron, O: red balls, W: turquoise balls, Se: bright green balls, P: pink balls, H: gray, Ce: yellow balls).

4642 | *Inorg. Chem. Front.*, 2020, **7**, 4640–4651

This journal is © the Partner Organisations 2020

Na$^+$ cations, 12 [H$_2$N(CH$_3$)$_2$]$^+$ cations, and 44 lattice water molecules. In detail, **1a** can be deemed as one trivacant Dawson [HPSeW$_{15}$O$_{54}$]$^{10-}$ (**1b**) segment containing mixed P^{III} and Se^{IV} HAs (Fig. 2b) and two trivacant Keggin [B-α-SeW$_9$O$_{33}$]$^{8-}$ segments (Fig. 2c) bridged by a hexanuclear heterometallic [Ce$_2$(H$_2$O)(W$_4$O$_9$)]$^{12+}$ cluster (Fig. 2d). All the W^{VI} centers displayed the octahedral coordination geometry [W–O: 1.659(17)–2.526(17) Å, ∠O–W–O: 67.0(6)–176.3(9)°]. Noticeably, a fresh Dawson **1b** segment can be considered as a combination of a hypothetical hexavacant Keggin [HPW$_6$O$_{21}$]$^{2-}$ subunit (Fig. 2e) and the trivacant Keggin [B-α-SeW$_9$O$_{33}$]$^{8-}$ subunit (Fig. 2f). It can be explicitly seen from the ball-and-stick view of the trivacant Dawson **1b** segment (Fig. 2g) that six {WO$_6$} octahedra at the unsealed end of the [B-α-SeW$_9$O$_{33}$]$^{8-}$ segment are connected with six {WO$_6$} octahedra of the [HPW$_6$O$_{21}$]$^{2-}$ subunit by sharing six μ$_2$-O atoms. It should be pointed out that the **1b** segment comprises two types of Has: one is the P^{III} atom with the {HPO$_3$} tetrahedral configuration, which is centrally located and connected to three O atoms (P–O: 1.501(15)–1.559(16) Å, P–H: 1.400(10), ∠O–P–O: 111.0(9)–112.2(9)°, ∠O–P–H: 95(10)–120(10)°, Fig. 2h), the other is the Se^{IV} atom with the {SeO$_3$} trigonal pyramidal geometry [Se–O: 1.660(15)–1.715(17) Å, ∠O–Se–O: 95.7(9)–101.9(8)°] (Fig. 2i). The simplified connection mode of the [Ce$_2$(H$_2$O)(W$_4$O$_9$)]$^{12+}$ cluster is depicted in Fig. 2j, in which Ce1, Ce2, W18, W19, and W5 centers form a distorted trigonal bipyramid (Fig. 2k). Among them, the W6 center hangs on the W5 and Ce2 centers. Both Ce1^{3+} and Ce2^{3+} cations are eight-coordinate and connected with each other via four Ce–O–W–O–Ce bonds (Ce1–O19–W6–O46–Ce2, Ce1–O118–W18–O74–Ce2, Ce1–O47–W19–O114–Ce2, Ce1–O19–W6–O4–W5–O2–Ce2), giving birth to the [Ce$_2$(H$_2$O)(W$_4$O$_9$)]$^{12+}$ cluster. Both Ce1^{3+} and Ce2^{3+} cations reside in a distorted bicapped trigonal prismatic geometry (Fig. 2l). The bicapped trigonal prism of the Ce1^{3+} cation is constituted by three O atoms (O19, O47, O118) from the [W$_4$O$_9$]$^{6+}$ fragment [Ce–O: 2.428(16)–2.508(14) Å], two atoms (O71, O119) from one trivacant [B-α-SeW$_9$O$_{33}$]$^{8-}$ segment [Ce–O: 2.463(15)–2.479(16) Å], and three coordinated water O atoms (O1 W, O2 W, O3 W) [Ce–O: 2.47(2)–2.57(2) Å], while the eight-coordinate Ce2^{3+} cation bonds to four O atoms (O2, O46, O74, O114) from the [W$_4$O$_9$]$^{6+}$ unit [Ce–O: 2.390(16)–2.528(16) Å], two O atoms (O76, O78) from the other trivacant [B-α-SeW$_9$O$_{33}$]$^{8-}$ cluster [Ce–O: 2.488(16)–2.503(17) Å], and two aqua molecules (O4 W, O5 W) [Ce–O: 2.453(17)–2.537(19) Å]. The cap sites are respectively occupied by two aqua molecules O1 W and O3 W for the Ce1^{3+} cation, and one O2 atom and one O4 W water molecule for the Ce2^{3+} cation. The bond valence sum (BVS) calculations of the bridging oxygen atoms and coordinated water molecules on Ce1^{3+} and Ce2^{3+} ions in **1** are given in the ESI (Table S2†).

Albeit RECHPOMs with two types of HA-inserted POM building blocks haven't been addressed to date, some HPOMs containing different POM building blocks have been sporadically reported. For example, in 2014, Cronin et al. presented a seductive multi-Pd^{II}-incorporated ST [H$_{12}$Pd$_{10}$Se$_{10}$W$_{52}$O$_{206}$]$^{28-}$ (Fig. 3a) comprising one tetravacant Dawson [Se$_2$W$_{14}$O$_{52}$]$^{12-}$
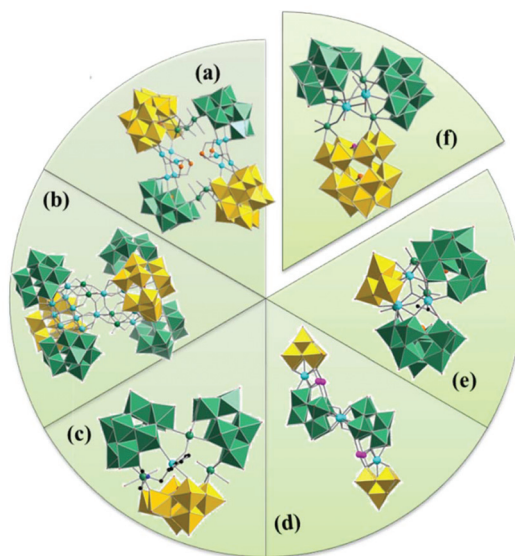
Fig. 3 (a) The multi-Pd^{II} incorporated ST [H$_{12}$Pd$_{10}$Se$_{10}$W$_{52}$O$_{206}$]$^{28-}$. (b) The largest Zr$_{24}$-cluster included in GT [Zr$_{24}$O$_{22}$(OH)$_{10}$(H$_2$O)$_2$(W$_2$O$_{10}$H)$_2$(GeW$_9$O$_{34}$)$_4$ (GeW$_8$O$_{31}$)$_2$]$^{32-}$. (c) The organoantimony(III)-functionalized AT [{2-(Me$_2$HN$^+$CH$_2$)C$_6$H$_4$Sb^{III}} {WO$_2$(H$_2$O)} {WO(H$_2$O)}$_2$(B-β-AsW$_8$O$_{30}$)(B-α-AsW$_9$O$_{33}$)$_2$]$^{14-}$. (d) The S-shaped tetrameric RE−organotin encapsulated TT {[RE$_2$(OH)(B-α-TeW$_7$O$_{28}$)Sn$_2$(CH$_3$)$_4$(W$_5$O$_{18}$)]$_2$}$^{14-}$. (e) The trimeric trinuclear-Zr^{IV} substituted TA {[Zr$_3$(OAc)W$_7$(H$_2$O)O$_{25}$][B-α-SbW$_9$O$_{33}$]$_2$}$^{15-}$. (f) The **1a** POA.

and two trivacant Keggin [B-α-SeW$_9$O$_{33}$]$^{8-}$ fragments.[38] In the same year, Yang's group discovered the largest Zr$_{24}$-cluster-inserted germanotungstate (GT) [Zr$_{24}$O$_{22}$(OH)$_{10}$(H$_2$O)$_2$ (W$_2$O$_{10}$H)$_2$(GeW$_9$O$_{34}$)$_4$ (GeW$_8$O$_{31}$)$_2$]$^{32-}$ (Fig. 3b) under hydrothermal conditions, which was built by four trilacunary Keggin [B-α-GeW$_9$O$_{34}$]$^{10-}$ and two tetralacunary Keggin [B-α-GeW$_8$O$_{31}$]$^{10-}$ subunits bridged by an S-shaped [Zr$_{24}$O$_{22}$(OH)$_{10}$(H$_2$O)$_2$]$^{42+}$ cluster.[39] In 2016, an organoantimony (III)-functionalized trimeric AT [{2-(Me$_2$HN$^+$CH$_2$)C$_6$H$_4$Sb^{III}} {WO$_2$(H$_2$O)}{WO(H$_2$O)}$_2$(B-β-AsW$_8$O$_{30}$)(B-α-AsW$_9$O$_{33}$)$_2$]$^{14-}$ was reported by Kortz's group, which was composed of one [B-β-AsW$_8$O$_{30}$]$^{9-}$ and two [B-α-AsW$_9$O$_{33}$]$^{9-}$ segments (Fig. 3c).[40] In 2018, a family of novel S-shaped tetrameric RE-organotin-encapsulated TTs {[RE$_2$(OH)(B-α-TeW$_7$O$_{28}$)Sn$_2$(CH$_3$)$_4$(W$_5$O$_{18}$)]$_2$}$^{14-}$ (RE = Er^{3+}, Yb^{3+}, Ho^{3+}, Y^{3+}) were found through the one-step self-assembly strategy by our lab, which encompassed two pentavacant Keggin [B-α-TeW$_7$O$_{28}$]$^{12-}$ and two monovacant Lindqvist [W$_5$O$_{18}$]$^{6-}$ entities joined by RE ions and dimethyltin groups (Fig. 3d).[41] In 2019, Yang et al. synthesized a novel trinuclear-Zr^{IV}-substituted TA {[Zr$_3$(OAc)W$_7$(H$_2$O)O$_{25}$][B-α-SbW$_9$O$_{33}$]$_2$}$^{15-}$ consisting of one divacant Lindqvist [W$_4$O$_{16}$]$^{8-}$ and two trivacant Keggin [B-α-SbW$_9$O$_{33}$]$^{9-}$ fragments (Fig. 3e).[42] Emphatically, **1a** was built by three kinds of different POM units, namely, one P^{III}-and-Se^{IV} co-inbuilt trilacunary Dawson [HPSeW$_{15}$O$_{54}$]$^{10-}$ segment, two trilacunary Keggin [B-α-SeW$_9$O$_{33}$]$^{8-}$ fragments, and one Ce^{III}–W^{III} heterometal [Ce$_2$(H$_2$O)(W$_4$O$_9$)]$^{12+}$ cluster (Fig. 3f). It should be noted that **1a** represents the first P^{III}-and-Se^{IV} co-inbuilt RECHPOM containing three kinds of different POM units.
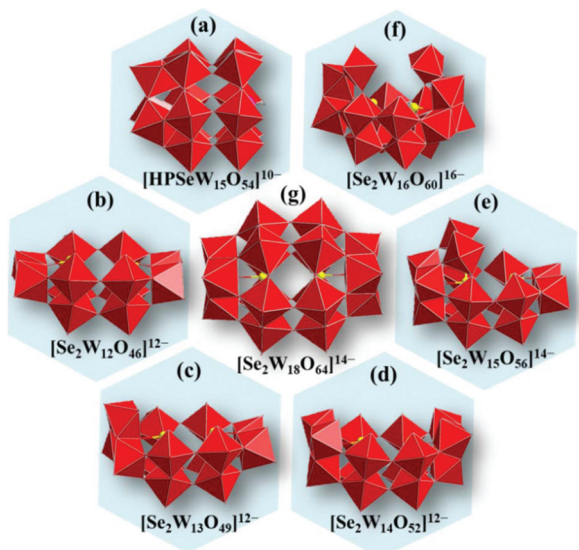
This journal is © the Partner Organisations 2020

Inorg. Chem. Front., 2020, 7, 4640–4651 | **4643**

Fig. 4 Some typical Dawson-type ST fragments: (a) $[HPSeW_{15}O_{54}]^{10-}$, (b) $[Se_2W_{12}O_{46}]^{12-}$, (c) $[Se_2W_{13}O_{49}]^{12-}$, (d) $[Se_2W_{14}O_{52}]^{12-}$, (e) $[Se_2W_{15}O_{56}]^{14-}$, (f) $[Se_2W_{16}O_{60}]^{16-}$, (g) $[Se_2W_{18}O_{64}]^{12-}$.

The P^{III}-and-Se^{IV} co-inbuilt trilacunary Dawson segment **1b** takes after the $[HPSeW_{15}O_{54}]^{10-}$ (Fig. 4a) observed in the cross-shaped clusters $[(XYW_{15}O_{54})_4(WO_2)_4]^{32-/36-}$ (X = HP^{III}, Y = Se^{IV}, Te^{IV}, As^{III}) reported by Cronin's group in 2014,[33] but has never been seen in other RECHPOMs. Up to now, some additional lacunary Dawson ST segments have also been discovered, such as $[Se_2W_{12}O_{46}]^{12-}$ (Fig. 4b) in $[Se_6W_{38}O_{132}(OH)_6(H_2O)_2]^{18-}$, $[Se_2W_{13}O_{49}]^{12-}$ (Fig. 4c) in $[Gd_4Se_6W_{48}O_{166}(H_2O)(OH)_4]^{20-}$, $[Se_2W_{14}O_{52}]^{12-}$ (Fig. 4d) in $[SeO_4RE_5(H_2O)_7(Se_2W_{14}O_{52})_2]^{12-}$ (RE = Dy^{3+}, Gd^{3+}), $[Se_2W_{15}O_{56}]^{14-}$ (Fig. 4e) in $[\{Sn(CH_3)_2\}_4\{Sn(CH_3)_2(H_2O)\}_2\{Sn(CH_3)_2(H_2O)_2\}$ $Se_8W_{54}O_{191}(OH)_7(H_2O)_2]^{19-}$, $[Se_2W_{16}O_{60}]^{16-}$ (Fig. 4f) in $[RE_4Se_8W_{56}O_{196}(H_2O)_{10/12}(OH)_{10}]^{22-}$ (RE = Gd^{3+}, Tb^{3+}, Dy^{3+}), and $[Se_2W_{18}O_{64}]^{12-}$ (Fig. 4g) in $[\{Sn(CH_3)_2(CH_3COO)\}_3\{Sn(CH_3)_2\}_3\{Se_2W_{18}O_{62}(OH)(H_2O)\}_3]^{18-}$.[32,43–46] What is worth mentioning is that these lacunary Dawson ST segments are derived from the plenary Dawson-like $[Se_2W_{18}O_{60}]^{6-}$ POA by the removal of some $\{WO_6\}$ octahedra in the equatorial or/and polar positions. Specifically, **1b** is formed by taking away from three $\{WO_6\}$ octahedra in the polar positions of the hypothetical Dawson-like $[HPSeW_{18}O_{60}]^{6-}$ POA, which is rarely seen in RECHPOMs. The discovery of **1b** not only greatly enriches the structural diversity of Dawson-type HPOM clusters, but also demonstrates that **1b** can be promisingly used as a POM building block to design and develop more much novel structures.

The 3D supramolecular packing structure of **1** can be constructed by hydrogen-bonding interactions and electrostatic attraction interactions between protonated $[HDMA]^+$ cations, lattice water molecules, and **1a** POAs. In order to clearly view the packing structure of **1**, Na^+ and $[NH_2(CH_3)]^+$ counter-cations and lattice water molecules distributed in the inter-space were removed, and the stacking representation of **1a** POAs viewed along the *b* axis is illustrated in Fig. 5a, where it

can be clearly obviously seen that **1a** POAs are orderly aligned in the staggered fashion in the –ABAB– mode along the *c* axis to enhance the stability of the structure. In order to make the 3D packing structure of **1** clearly visible, each **1a** POA was simplified as a triangle (Fig. 5b), which further highlighted the –ABAB– stacking mode of **1a** POAs. The unambiguous array patterns of **1a** POAs in layer A and layer B are shown in Fig. 5c and d, where clearly, **1a** POAs in both layers display the –AAA– packing mode. In addition, there are two types of arrangement modes (named as type I and type II) between neighboring layer A and layer B (Fig. 5e and f). In type I (Fig. 5g and h), layer A and layer B are heaped in a "shoulder to shoulder" motif; whereas, in type II (Fig. 5i and j), layer A and layer B are heaped in a "head to head" pattern. On the whole, the simplified diagram of the 3D packing structure of **1** is simple and straightforward, and more clearly describes the stacking pattern of –ABAB– or –AAA–. The packing diagrams of **1a** along the *a* axis and *c* axis are revealed in Fig. S4 and 5.†

Electrochemical sensing properties

The electrochemical detection of small bioactive molecules, such as dopamine, uric acid, and ascorbic acid, in the human body has aroused great attention in analytical chemistry and the clinical medicine fields.[47–53] As an important neurotransmitter in the brain, DA is involved in many physiological and clinical activities of humans and mammals. Previous studies have proved that DA has momentous medicinal value in treating Parkinson's disease, depression, shock (including toxic shock, cardiogenic shock, hemorrhagic shock and central shock) and so on.[35,54] In addition, UA is the end product of purine metabolism in the human body and it has a rather energetic antioxidant ability and plays a key role in guaranteeing the normal function of cells. The excretion imbalance of UA, resulting in an elevated UA content in blood, is the main cause of gout.[55–58] Therefore, searching for a swift and straightforward detection method to determine DA and UA has long been a focus in related fields. Currently, electrochemical detection toward DA or UA has been applied on account of its high sensitivity, operational briefness, fast response, and low cost. The oxidation potentials of DA and UA are similar and it is difficult to separate them; therefore, it is still challenging to detect DA and UA at the same time.[59] Due to the structural diversity and good redox performances, POMs have attracted considerable interest in the sensing field,[60] while the conductivity of the POM-based sensors remains a critical problem to be solved. As is well-known, CMWCNTs, benefiting from their high electrical conductivity, have often been studied to modify electrodes so as to improve their electrochemical performance, elevate the response signal, and enhance the sensitivity of detecting biological targets. Therefore, considering that POMs can potentially act as efficient donors or acceptors of electrons without structural change, **1** was used to fabricate an ECS and its electrochemical response was evaluated toward the simultaneous detection of DA and UA. Specifically, the complex of **1** and CMWCNT was dropped onto GCE forming **1**@CMWCNT-GCE. The electrochemical responses of the
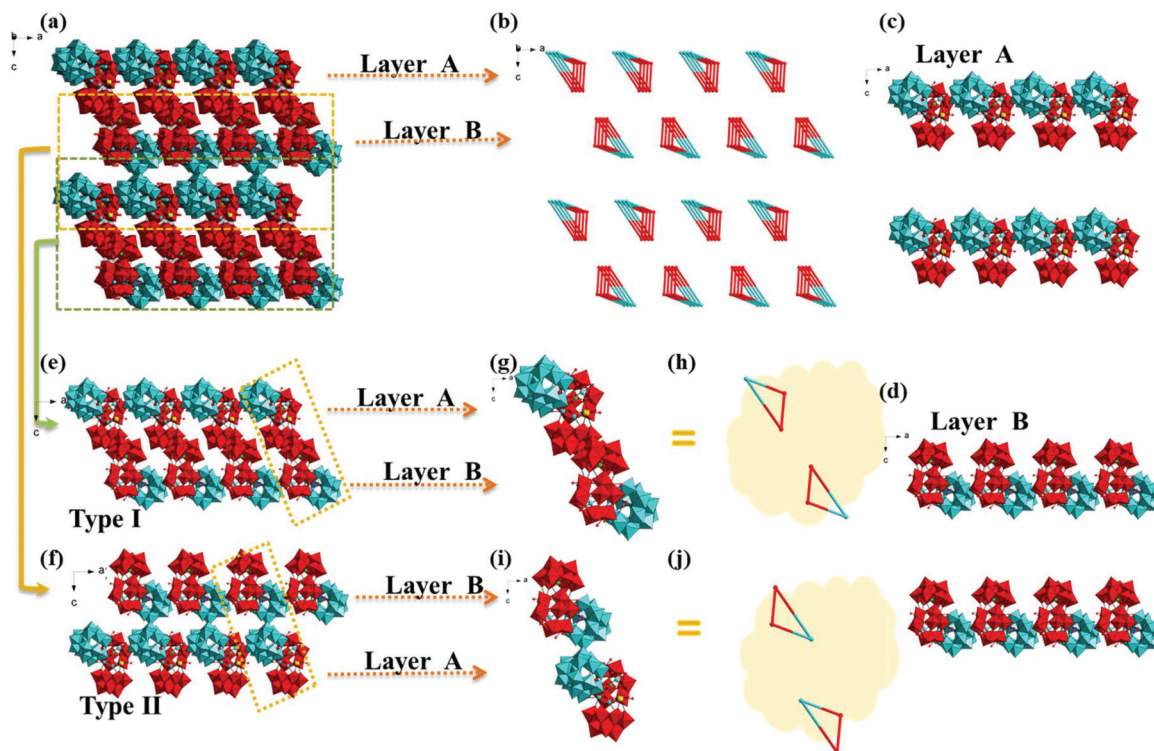
Fig. 5 (a) The **1a** POA. (b) The trivacant Dawson-type **1b** segment. (c) The trivacant Keggin $[B-\alpha-SeW_9O_{33}]^{8-}$ fragment. (d) View of the $[Ce_2(H_2O)(W_4O_9)]^{12+}$ cluster in **1a**. (e) The hypothetical hexavacant Keggin $[HPW_6O_{21}]^{2-}$ subunit in **1b**. (f) The trivacant Keggin $[B-\alpha-SeW_9O_{33}]^{8-}$ subunit in **1b**. (g) Connection motif between the $[B-\alpha-SeW_9O_{33}]^{8-}$ subunit and $[HPW_6O_{21}]^{2-}$ subunit in **1b**. (h) The tetrahedral geometry of the $\{HPO_3\}$ group in **1b**. (i) The trigonal pyramidal geometry of the $\{SeO_3\}$ group in **1b**. (j) The simplified connection mode of the $[Ce_2(H_2O)(W_4O_9)]^{12+}$ cluster. (k) Distorted trigonal bipyramid of $\{Ce_2W_3\}$. (l) The coordination geometry of $Ce1^{3+}$ and $Ce2^{3+}$ ions. (W: Red and turquoise octahedron, O: red balls, W: turquoise balls, Se: bright green balls, P: pink balls, H: gray, Ce: yellow balls).

1@CMWCNT-GCE ECS to detect DA and UA were further studied by cyclic voltammetry (CV) in 0.10 mol L^{-1} PBS (pH 7.00). The idiographic preparation process of **1**@CMWCNT-GCE ECS is revealed in the ESI,† while schematics of the preparation route and possible detection response mechanism are displayed in Fig. 6.

In order to probe the stability of **1** in aqueous solution, the UV spectral evolution of **1** in aqueous solution with the pH varying from 1.00 to 10.00 was measured (Fig. S6†), which indicated that **1** was stable in the pH range of 3.00–8.00. As a result, the CV responses of **1**@CMWCNT-GCE to 1.00 mmol L^{-1} DA or 1.00 mmol L^{-1} UA in 0.10 mol L^{-1} PBS solution (pH 7.00) were investigated (Fig. 7a), and showed conspicuous CV response signals of **1**@CMWCNT-GCE to 1.00 mmol L^{-1} DA (purple line) or 1.00 mmol L^{-1} UA (red line) in 0.10 mol L^{-1} PBS solution, respectively, which can suggest that the simultaneous detection of **1**@CMWCNT-GCE for DA and UA may be feasible since two characteristic oxidation peaks derived from DA (0.19 V) and UA (0.38 V) could be easily distinguished.[61]

Then, CV curves of the bare GCE, CMWCNT-GCE, and **1**@CMWCNT-GCE in 0.10 mol L^{-1} PBS (pH 7.00) in the absence of DA and UA were respectively researched (Fig. S7†). From the results, no redox peak could be seen when the bare GCE was used, while a couple of weak redox waves with the oxi-
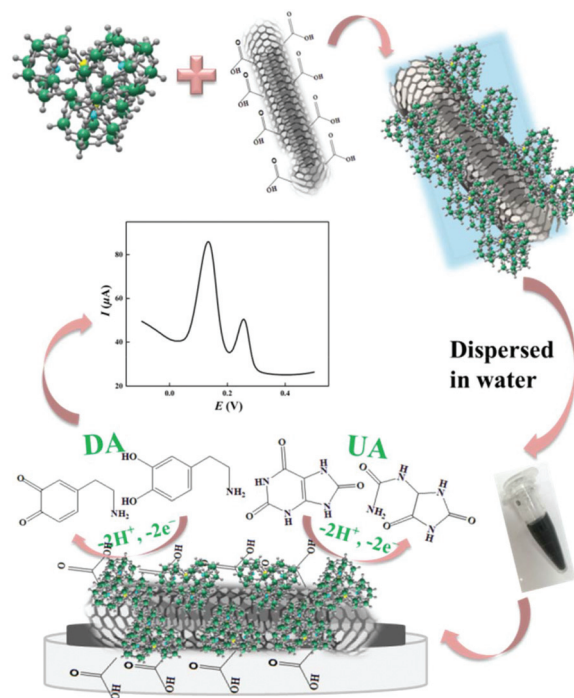

Fig. 6 Schematics of the fabrication of the **1**@CMWCNT-GCE ECS and possible detection response mechanism.
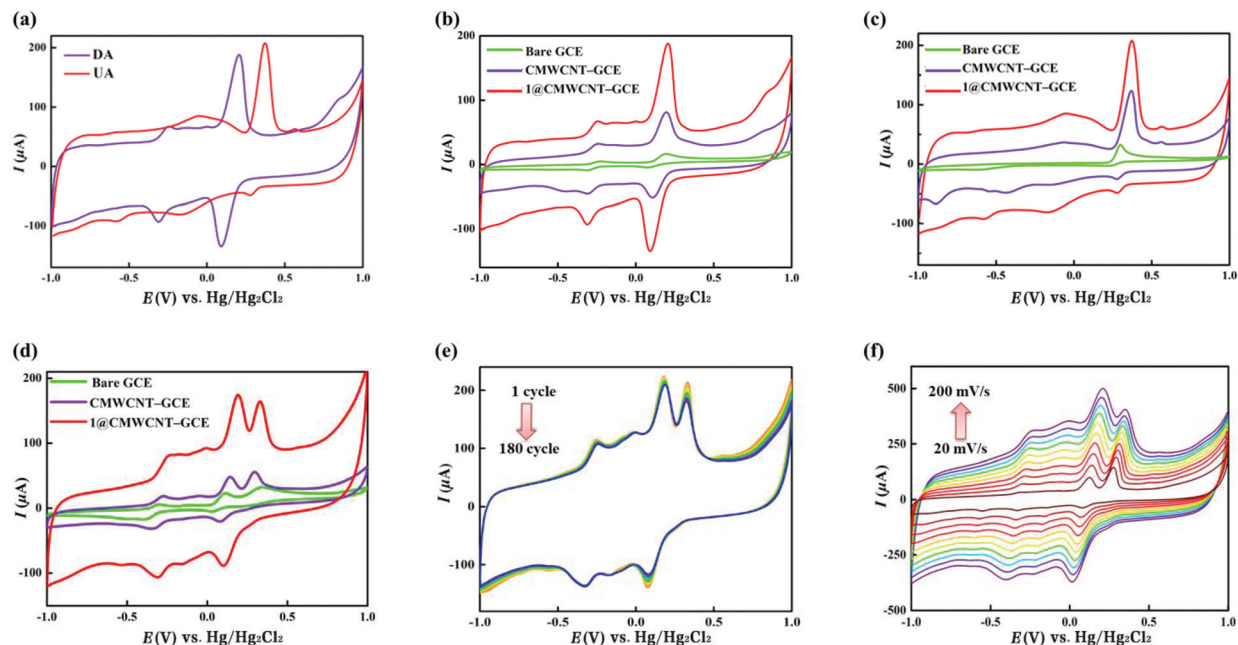
This journal is © the Partner Organisations 2020

Inorg. Chem. Front., 2020, **7**, 4640–4651 | **4645**

Fig. 7 (a) CV response curves of **1**@CMWCNT-GCE in 0.10 mol L^{-1} PBS solution (pH 7.00) containing 1.00 mmol L^{-1} DA or 1.00 mmol L^{-1} UA. (b) Comparison of CVs of bare GCE, CMWCNT-GCE, and **1**@CMWCNT-GCE in 0.10 mol L^{-1} PBS solution (pH 7.00) containing 1.00 mmol L^{-1} DA. (c) Comparison of CVs of bare GCE, CMWCNT-GCE, and **1**@CMWCNT-GCE in 0.10 mol L^{-1} PBS solution (pH 7.00) containing 1.00 mmol L^{-1} UA. (d) Comparison of CVs of bare GCE, CMWCNT-GCE, and **1**@CMWCNT-GCE in 0.10 mol L^{-1} PBS solution (pH 7.00) containing 1.00 mmol L^{-1} DA and 1.00 mmol L^{-1} UA. (e) CV curves of **1**@CMWCNT-GCE from the first round to the 180th round in 0.10 mol L^{-1} PBS (pH 7.00) solution containing 1.00 mmol L^{-1} DA and 1.00 mmol L^{-1} UA. (f) CV curves of **1**@CMWCNT-GCE in the 0.10 mol L^{-1} PBS solution containing 1.00 mmol L^{-1} DA and 1.00 mmol L^{-1} UA at different scan rates.

dation peak potential of +0.02 V and reduction peak potential of −0.42 V, which resulted from the redox process of CMWCN, could be observed by using CMWCNT-GCE. By contrast, when **1**@CMWCNT-GCE was employed, one newly emerged oxidation peak at −0.09 V and one reduction peak at −0.16 V in the CV curve could be assigned to the redox process of the W^{VI} centers in **1** (Fig. S7†).[35,62] Subsequently, the CV responses of the bare GCE, CMWCNT-GCE, and **1**@CMWCNT-GCE were measured in 0.10 mol L^{-1} PBS (pH 7.00) in the presence of 1.00 mol L^{-1} DA or UA, respectively (Fig. 7b and c). The CV curves measured in PBS containing 1.00 mol L^{-1} DA presented two apparent oxidation peaks around +0.19 and −0.24 V and two corresponding reduction peaks around +0.08 and −0.31 V, which could be attributed to the redox process of DA (Fig. 7b).[51,63,64] There is no doubt that the appearance of the strongest oxidation and reduction peaks of DA when **1**@CMWCNT-GCE was applied as the working electrode demonstrated that **1**@CMWCNT-GCE may be a valuable choice for the electrochemical detection of DA. Similarly, Fig. 7c shows the presence of a strong oxidation peak at 0.38 V and a corresponding reduction peak at 0.28 V, resulting from the oxidation–reduction process of UA.[65] It can be clearly seen from the above comparison that the current intensities of the redox peaks of DA or UA taken by using **1**@CMWCNT-GCE were dramatically enhanced compared with those obtained by CMWCNT-GCE or bare GCE, which indicates that **1** plays a signal amplification role in improving the sensing perform-

ance of **1**@CMWCNT-GCE. Considering such a promising potential of **1**@CMWCNT-GCE in a single-component detection process for either DA or UA, it is believed that the simultaneous detection of two or even more small biomolecules (*e.g.*, DA and UA) is worthy of being studied.

Thus, the CV responses of bare GCE, CMWCNT-GCE, and **1**@CMWCNT-GCE to 0.10 mol L^{-1} PBS solution simultaneously containing DA and UA (c(DA or UA) = 1.00 mmol L^{-1}) in the voltage range of −1.00–1.00 V at a scan rate of 100 mV s^{-1} were tested (Fig. 7d). The test results demonstrated that **1**@CMWCNT-GCE indeed showed remarkably stronger CV oxidation signals of DA (0.19 V) and UA (0.34 V) than either bare GCE or CMWCNT-GCE. This phenomenon certified that **1**@CMWCNT-GCE can serve as an ECS to simultaneously detect DA and UA in PBS solution. Therefore, it is believed that **1a** POAs in **1**@CMWCNT-GCE behave as a signal amplifier in the electrochemical sensing process. The sensing mechanism of the **1**@CMWCNT-GCE ECS toward detecting UA and DA can be speculated as follows: (i) hydrogen-bonding, electrostatic attraction, and physisorption interactions between DA/UA and the **1**@CMWCNT ECS provide the preconditions for the redox response on the electrode, whereby the loading of **1** on CMWCNT-GCE accelerated the electron transfer rate;[48–50] (ii) the synergistic effect of **1** as a signal-amplifier and CMWCNT as a conductivity enhancer facilitates a good sensing performance of the **1**@CMWCNT-GCE ECS for detecting DA and UA.[66]
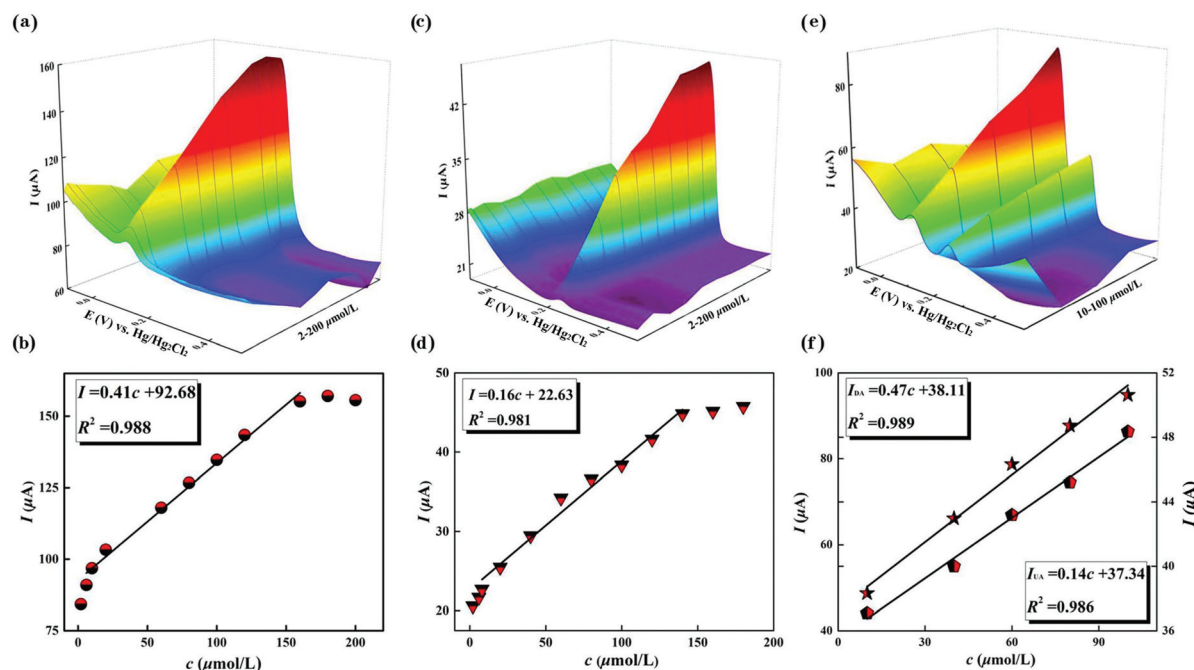
Fig. 8 (a) DPV curves of **1**@CMWCNT-GCE with the DA concentration varying in the range of 2–200 μmol L^{-1}. (b) The linear relationship between the peak current of DA and its concentration. (c) DPV curves of **1**@CMWCNT-GCE with the UA concentration varying in the range of 2–200 μmol L^{-1}. (d) The linear relationship between the peak current of UA and its concentration. (e) DPV curves of **1**@CMWCNT-GCE with the DA and UA concentration varying in the range of 10–100 μmol L^{-1}. (f) The linear relationship between the peak currents of DA and UA and their concentrations.

So as to examine the stability of the **1**@CMWCNT-GCE ECS, the working process of the **1**@CMWCNT-GCE ECS toward detecting DA and UA was monitored by CV measurements for 180 cycles in 0.10 mol L^{-1} PBS solution including 1.00 mmol L^{-1} DA and 1.00 mmol L^{-1} UA (pH 7.00). It can be seen from Fig. 7e that the peak current and peak potential were slightly changed, which testifies that the **1**@CMWCNT-GCE ECS exhibited excellent stability during the detection. Compared with DA, although the peak current of UA was decreased a little, the peak current for the 180th cycle for UA still declined by no more than 15% in contrast to the 1st peak current, which can meet the need for the detection.

The effect of the scan rate on the CV curves for the **1**@CMWCNT-GCE ECS in the sensing process of DA and UA was also investigated with the scan rate varying from 20 to 200 mV s^{-1} (Fig. 7f). This showed that the peak currents of DA and UA increased gradually with the increasing of scan rate. The linear equation of the oxidation peak current of DA and the scan rate is I_{pa} (μA) = 2.21ν (mV s^{-1}) + 73.95 with R^2 = 0.995 (*I*: peak current, Fig. S8†), while the linear function of the oxidation peak current of UA and scan rate is I_{pa} (μA) = 1.40ν (mV s^{-1}) + 135.34 with R^2 = 0.995 (Fig. S9†), indicating that the electrochemical sensing procedure is surface-controlled.[54]

In addition, differential pulse voltammetry (DPV) was also adopted to study the detection of the **1**@CMWCNT-GCE ECS toward DA and UA. First, DPV response curves of the **1**@CMWCNT-GCE ECS in 0.10 mol L^{-1} PBS (pH 7.00) with the change in the concentration of DA or UA (*c* = 2–200 μmol L^{-1})

were detected. Fig. 8a shows that the peak current (*I*) gradually increased with the elevation of the DA concentration (*c*) at 10–160 μmol L^{-1}, showing a good linear relationship in the DA concentration range of 10–160 μmol L^{-1}. The relationship between *I* and *c* could be fitted using the linear regression equation of I_{DA} (μA) = 0.41c (μmol L^{-1}) + 92.68 (R^2 = 0.988) (Fig. 8b) (R^2: the linear correlation). The limit of determination (LOD) of the **1**@CMWCNT-GCE ECS toward DA was calculated to be 1.85 μmol L^{-1} (LOD = 3σ/k, σ: the standard deviation, *k*: the slope of the linear equation). Fig. 8c reveals the peak current increased in proportion to the UA concentration in the range of 8–140 μmol L^{-1} and it could be fitted by I_{UA} (μA) = 0.16c (μmol L^{-1}) + 22.63 (R^2 = 0.981, *c*: the concentration of UA) (Fig. 8d). The LOD of the **1**@CMWCNT-GCE ECS toward UA was calculated to be 4.73 μmol L^{-1}. The good linear relation between the peak current and the concentration of DA or UA demonstrated that the **1**@CMWCNT-GCE ECS was suitable for examining DA and UA in the aforesaid concentration range. These results suggest that the peak currents increased gradually and showed a good linear relationship when DA and UA were detected by the above method, indicating that it is feasible to discuss the concentrations of these two small molecules simultaneously.

Then, the **1**@CMWCNT-GCE ECS was used to simultaneously detect the peak currents of DA and UA (*c*(DA : UA) = 1 : 1) in different concentrations. As can be seen from Fig. 8e, when the total concentration of DA and UA increased in the range of 10–100 μmol L^{-1}, their peak currents gradually rose

This journal is © the Partner Organisations 2020

Inorg. Chem. Front., 2020, **7**, 4640–4651 | **4647**

and showed a good linear relationship between I and c, which could be fitted by the linear regression equation of I_{DA} (μA) = 0.47c (μmol L^{-1}) + 38.11 (R^2 = 0.989) for detecting DA and I_{UA} (μA) = 0.14c (μmol L^{-1}) + 37.34 (R^2 = 0.986) (Fig. 8f) for detecting UA. Therefore, the LODs of DA and UA when **1**@CMWCNT-GCE served as the ECS were calculated to be 1.61 and 5.41 μmol L^{-1}, respectively. Although the linear range decreased in the two-component detection process, the linear relationship between the peak current and the concentration was still pretty good, which shows the good opportunity for developing **1**@CMWCNT-GCE ECS as an efficient biosensor to detect small biomolecules in biological environments.

Conclusions

In conclusion, a series of mixed P^{III} and Se^{IV} heteroatom-oriented RE-embedded HPOTs **1–8** were first prepared in aqueous solution through the self-assembly reaction strategy. The most noteworthy architectural feature of **1–8** is that their POA backbones concurrently comprised two trivacant Keggin-type Se^{IV}-inserted [B-α-SeW$_9$O$_{33}$]$^{8-}$ segments and one trivacant Dawson-type P^{III}-and-Se^{IV}-inserted [HPSeW$_{15}$O$_{54}$]$^{10-}$ segment joined by a hexanuclear heterometallic [RE$_2$(H$_2$O)(W$_4$O$_9$)]$^{12+}$ cluster, which represent the first RECHPOMs including two types of HAs. This study consolidates the notion that it is highly feasible to synchronously introduce two or even more kinds of HAs into the RECHPOM system, which lays a firm foundation for designing and synthesizing more novel HPOM-based materials. Moreover, **1**@CMWCNT-GCE could work as an ECS for the detection of DA and UA and showed a good stability and a low detection limit, demonstrating the application potential of **1** in the electrochemical biosensing field. Also, this work will drive further study on multi-HA-inserted POMs in the future.

Conflicts of interest

There are no conflicts to declare.

Acknowledgements

Notes and references

1 S. Omwoma, C. T. Gore, Y. C. Ji, C. W. Hu and Y. F. Song, Environmentally benign polyoxometalate materials, *Coord. Chem. Rev.*, 2015, **286**, 17–29.
2 A. Proust, R. Thouvenot and P. Gouzerh, Interconnected porous nanoflakes of CoMo$_2$S$_4$ as an efficient bifunctional electrocatalyst for overall water electrolysis, *Chem. Commun.*, 2008, 1837–1852.
3 J. Zhou, J.-W. Zhao, Q. Wei, J. Zhang and G. Y. Yang, Two tetra-Cd^{II}-substituted vanadogermanate frameworks, *J. Am. Chem. Soc.*, 2014, **136**, 5065–5071.
4 J. Yan, D.-L. Long and L. Cronin, Development of a building block strategy to access gigantic nanoscale heteropolyoxotungstates by Using SeO$_3$$^{2-}$ as a template linker, *Angew. Chem., Int. Ed.*, 2010, **49**, 4117–4120.
5 C. Boskovic, Rare earth polyoxometalates, *Acc. Chem. Res.*, 2017, **50**, 2205–2214.
6 C. H. Zhan, Q. Zheng, D.-L. Long, L. Vilà-Nadal and L. Cronin, Controlling the reactivity of the [P$_8$W$_{48}$O$_{184}$]$^{40-}$ inorganic ring and its assembly into POMZite inorganic frameworks with silver ions, *Angew. Chem., Int. Ed.*, 2019, **58**, 17282–17286.
7 A. Müller, F. Peters, M. T. Pope and D. Gatteschi, Polyoxometalates: very large clusters–nanoscale magnets, *Chem. Rev.*, 1998, **98**, 239–270.
8 L. Cheng, L. Niu, J. Gong and S. J. Dong, Electrochemical growth and characterization of polyoxometalate-containing monolayers and multilayers on alkanethiol monolayers self-assembled on gold electrodes, *Chem. Mater.*, 1999, **11**, 1465–1475.
9 Y. J. Liu, M. T. Jin, L. J. Chen and J. W. Zhao, Recent advances in isopolyoxotungstates and their derivatives, *Acta Crystallogr., Sect. C: Struct. Chem.*, 2018, **74**, 1202–1221.
10 J. Gao, J. Yan, S. G. Mitchell and H. N. Miras, Self-assembly of a family of macrocyclic polyoxotungstates with emergent material properties, *Chem. Sci.*, 2011, **2**, 1502–1508.
11 D. Wang, L. L. Liu, J. Jiang, L. J. Chen and J. W. Zhao, Polyoxometalate-based composite materials in electrochemistry: state-of-the-art progress and future outlook, *Nanoscale*, 2020, **12**, 5705–5718.
12 K. Yonesato, H. Ito, H. Itakura, D. Yokogawa, T. Kikuchi, N. Mizuno, K. Yamaguchi and K. Suzuki, Controlled assembly synthesis of atomically precise ultrastable silver nanoclusters with polyoxometalates, *J. Am. Chem. Soc.*, 2019, **141**, 19550–19554.
13 I. V. Kalinina, E. V. Peresypkina, N. V. Izarova, F. M. Nkala, U. Kortz, N. B. Kompankov, N. K. Moroz and M. N. Sokolov, Cyclic tungstoselenites based on {Se$_2$W$_{12}$} units, *Inorg. Chem.*, 2014, **53**, 2076–2082.
14 W.-C. Chen, X.-L. Wang, Y.-Q. Jiao, P. Huang, E.-L. Zhou, Z.-M. Su and K.-Z. Shao, pH-controlled and sulfite anion-directed assembly of a family of cerium(III)-containing polyoxotungstates clusters, *Inorg. Chem.*, 2014, **53**, 9486–9497.
15 J.-C. Liu, Q. Han, L.-J. Chen, J.-W. Zhao, C. Streb and Y. F. Song, Aggregation of giant cerium-bismuth tungstate

clusters into a 3D porous framework with high proton conductivity, *Angew. Chem., Int. Ed.*, 2018, **57**, 8416–8420.

16 J. W. Zhao, H. L. Li, X. Ma, Z. G. Xie, L. J. Chen and Y. S. Zhu, Lanthanide-connecting and lone-electron-pair active trigonal-pyramidal-AsO$_3$ inducing nanosized poly (polyoxotungstate) aggregates and their anticancer activities, *Sci. Rep.*, 2016, **6**, 26406.

17 B. S. Bassil, M. H. Dickman, I. Römer, B. von der Kammer and U. Kortz, The tungstogermanate $[Ce_{20}Ge_{10}W_{100}O_{376}(OH)_4(H_2O)_{30}]^{56-}$: a polyoxometalate containing 20 cerium(III) atoms, *Angew. Chem., Int. Ed.*, 2007, **46**, 6192–6195.

18 Q. Han, J.-C. Liu, Y. Wen, L.-J. Chen, J.-W. Zhao and G.-Y. Yang, Tellurotungstate-based organotin–rare-earth heterometallic hybrids with four organic components, *Inorg. Chem.*, 2017, **56**, 7257–7269.

19 J. W. Zhao, Y. Z. Li, L. J. Chen and G. Y. Yang, Research progress on polyoxometalate-based transition-metal–rare-earth heterometallic derived materials: synthetic strategies, structural overview and functional applications, *Chem. Commun.*, 2016, **52**, 4418–4445.

20 K. Fukaya and T. Yamase, Alkali-metal-controlled self-assembly of crown-shaped ring complexes of lanthanide/[a-AsW$_9$O$_{33}$]$^{9-}$: $[K⊂\{Eu(H_2O)_2(a-AsW_9O_{33})\}_6]^{35-}$ and $[Cs⊂\{Eu(H_2O)_2(a-AsW_9O_{33})\}_4]^{23-}$, *Angew. Chem., Int. Ed.*, 2003, **42**, 654–658.

21 Y. Wang, X. P. Sun, S. Z. Li, P. T. Ma, J. Y. Niu and J. P. Wang, Generation of large polynuclear rare earth metal-containing organic–inorganic polytungstoarsenate aggregates, *Cryst. Growth Des.*, 2015, **15**, 2057–2063.

22 M. Sadakane, M. H. Dickman and M. T. Pope, Controlled assembly of polyoxometalte chains from lacunary building blocks and lanthanide-cation linkers, *Angew. Chem., Int. Ed.*, 2000, **39**, 2914–2916.

23 F. Hussain, R. W. Gable, M. Speldrich, P. Kögerler and C. Boskovic, Polyoxotungstate-encapsulated Gd$_6$ and Yb$_{10}$ complexes, *Chem. Commun.*, 2009, 328–330.

24 S. X. Shang, Z. G. Lin, A. S. Yin, S. Yang, Y. N. Chi, Y. Wang, J. Dong, B. Liu, N. Zhen, C. L. Hill and C. W. Hu, Self-assembly of Ln(III)-containing tungstotellurates(VI): correlation of structure and photoluminescence, *Inorg. Chem.*, 2018, **57**, 8831–8840.

25 W.-C. Chen, C. Qin, X.-L. Wang, Y. G. Li, H.-Y. Zang, K.-Z. Shao, Z.-M. Su and E.-B. Wang, Assembly of a large cerium(III)-containing tungstotellurites(IV) nanocluster: $[Ce_{10}Te_8W_{88}O_{298}(OH)_{12}(H_2O)_{40}]^{18-}$, *Dalton Trans.*, 2015, **44**, 11290–11293.

26 X. Xu, R. R. Meng, C. T. Lu, L. Mei, L. J. Chen and J. W. Zhao, Acetate-decorated tri-Ln(III)-containing antimonotungstates with a tetrahedral {WO$_4$} group as a structure-directing template and their luminescence properties, *Inorg. Chem.*, 2020, **59**, 3954–3963.

27 K. Wassermann, M. H. Dickman and M. T. Pope, Self-assembly of supramolecular polyoxometalates: the compact, water-soluble heteropolytungstate anion $[As^{III}_{12}Ce^{III}_{16}(H_2O)_{36}W_{148}O_{524}]^{76-}$, *Angew. Chem., Int. Ed. Engl.*, 1997, **36**, 1445–1448.

28 F. Hussain, F. Conrad and G. R. Patzke, A gadolinium–bridged polytungstoarsenate(III) nanocluster: $[Gd_8As_{12}W_{124}O_{432}(H_2O)_{22}]^{60-}$, *Angew. Chem., Int. Ed.*, 2009, **48**, 9088–9091.

29 W.-C. Chen, H.-L. Li, X.-L. Wang, K.-Z. Shao, Z.-M. Su and E.-B. Wang, Assembly of cerium(III)-stabilized polyoxotungstate nanoclusters with SeO$_3$$^{2-}$/TeO$_3$$^{2-}$ templates: from single polyoxoanions to inorganic hollow spheres in dilute solution, *Chem. – Eur. J.*, 2013, **19**, 11007–11015.

30 J. Cai, X.-Y. Zheng, J. Xie, Z.-H. Yan, X.-J. Kong, Y.-P. Ren, L.-S. Long and L.-S. Zheng, Anion-dependent assembly of heterometallic 3d–4f clusters based on a lacunary polyoxometalate, *Inorg. Chem.*, 2017, **56**, 8439–8445.

31 W.-C. Chen, C. Qin, Y.-G. Li, H.-Y. Zang, K.-Z. Shao, Z.-M. Su and E.-B. Wang, Assembly of large purely inorganic Ce-stabilized/bridged selenotungstates: from nanoclusters to layers, *Chem. – Asian J.*, 2015, **10**, 1184–1191.

32 W.-C. Chen, L.-K. Yan, C.-X. Wu, X.-L. Wang, K.-Z. Shao, Z.-M. Su and E.-B. Wang, Assembly of Keggin-/Dawson-type polyoxotungstate clusters with different metal units and SeO$_3$$^{2-}$ heteroanion templates, *Cryst. Growth Des.*, 2014, **14**, 5099–5110.

33 Q. Zheng, L. Vilà-Nadal, Z. L. Lang, J.-J. Chen, D.-L. Long, J. S. Mathieson, J. M. Poblet and L. Cronin, Self-sorting of heteroanions in the assembly of cross-shaped polyoxometalate clusters, *J. Am. Chem. Soc.*, 2018, **140**, 2595–2601.

34 Q. Zheng, M. Kupper, W. M. Xuan, H. Oki, R. Tsunashima, D.-L. Long and L. Cronin, Anisotropic polyoxometalate cages assembled via layers of heteroanion templates, *J. Am. Chem. Soc.*, 2019, **141**, 13479–13486.

35 Y. M. Li, H. L. Li, J. Jiang, L. J. Chen and J. W. Zhao, Three types of distinguishing L-alanine-decorated and rare-earth-incorporated arsenotungstate hybrids prepared in a facile one-step assembly strategy, *Inorg. Chem.*, 2019, **58**, 3479–3491.

36 H. L. Li, C. Lian, L. J. Chen, J. W. Zhao and G. Y. Yang, Two Ce^{3+}-substituted selenotungstates regulated by *N,N*-dimethylethanolamine and dimethylamine hydrochloride, *Inorg. Chem.*, 2019, **58**, 8442–8450.

37 H.-L. Li, Y.-J. Liu, J.-L. Liu, L.-J. Chen, J.-W. Zhao and G.-Y. Yang, Structural transformation from dimerization to tetramerization of serine-decorated rare-earth-incorporated arsenotungstates induced by the usage of rare-earth salts, *Chem. – Eur. J.*, 2017, **23**, 2673–2689.

38 J. M. Cameron, J. Gao, D. L. Long and L. Cronin, Self-assembly and structural transformations of high-nuclearity palladium-rich polyoxometalates, *Inorg. Chem. Front.*, 2014, **1**, 178–185.

39 L. Huang, S.-S. Wang, J.-W. Zhao, L. Cheng and G.-Y. Yang, Synergistic combination of multi-Zr^{IV} cations and lacunary Keggin germanotungstates leading to a gigantic Zr$_{24}$-cluster-substituted polyoxometalate, *J. Am. Chem. Soc.*, 2014, **136**, 7637–7642.

40 P. Yang, Z. G. Lin, G. Alfaro-Espinoza, M. S. Ullrich, C. I. Rat, C. Silvestru and U. Kortz, 19-tungstodiarsenate(III) functionalized by organoantimony(III) groups: tuning

This journal is © the Partner Organisations 2020

Inorg. Chem. Front., 2020, **7**, 4640–4651 | **4649**

the structure–bioactivity relationship, *Inorg. Chem.*, 2016, **55**, 251–258.

41 J.-L. Liu, M.-T. Jin, L.-J. Chen and J.-W. Zhao, First dimethyltin-functionalized rare-earth incorporated tellurotungstates consisting of {B-α-TeW$_7$O$_{28}$} and {W$_5$O$_{18}$} mixed-building units, *Inorg. Chem.*, 2018, **57**, 12509–12520.

42 H. L. Li, Z. Zhang, Y. L. Wang and G. Y. Yang, A trinuclear Zr-substituted decanuclear hetero-metal sandwich tungstoantimonate: synthesis, structure and properties, *Eur. J. Inorg. Chem.*, 2019, 486–491.

43 J. M. Cameron, J. Gao, L. Vilà-Nadal, D.-L. Long and L. Cronin, Formation, self-assembly and transformation of a transient selenotungstate building block into clusters, chains and macrocycles, *Chem. Commun.*, 2014, **50**, 2155–2157.

44 W.-C. Chen, C. Qin, Y.-G. Li, H.-Y. Zang, K. Z. Shao, Z. M. Su, E. B. Wang and H. S. Liu, Assembly of tetrameric dimethyltin-functionalized selenotungstates: from nanoclusters to one-dimensional chains, *Chem. Commun.*, 2015, **51**, 2433–2436.

45 W.-C. Chen, C. Qin, X.-L. Wang, C.-X. Wu, Y.-G. Li, H.-Y. Zang, K.-Z. Shao, Z.-M. Su and E.-B. Wang, Trimeric hexa-dimethyltin-functionalized selenotungstate [{Sn(CH$_3$)$_2$(CH$_3$COO)}$_3${Sn(CH$_3$)$_2$}$_3${Se$_2$W$_{18}$O$_{62}$(OH)(H$_2$O)}$_3$]$^{18-}$, *CrystEngComm*, 2016, **18**, 2820–2824.

46 W.-C. Chen, C.-Q. Jiao, X.-L. Wang, K.-Z. Shao and Z.-M. Su, Self-assembly of nanoscale lanthanoid-containing selenotungstates: synthesis, structures, and magnetic studies, *Inorg. Chem.*, 2019, **58**, 12895–12904.

47 N. Thakur, S. D. Adhikary, M. Kumar, D. Mehta, A. K. Padhan, D. Mandal and T. C. Nagaiah, Ultrasensitive and highly selective electrochemical detection of dopamine using poly(ionic liquids)–cobalt polyoxometalate/CNT composite, *ACS Omega*, 2018, **3**, 2966–2973.

48 A. Salimi, A. Korani, R. Hallaj and R. Khoshnavazi, Modification of glassy carbon electrode with single-walled carbon nanotubes and α-silicomolybdate: application to Sb(III) detection, *Electroanalysis*, 2008, **23**, 2509–2517.

49 C.-L. Sun, H.-H. Lee, J.-M. Yang and C.-C. Wu, The simultaneous electrochemical detection of ascorbic acid, dopamine, and uric acid using graphene/size-selected Pt nanocomposites, *Biosens. Bioelectron.*, 2011, **26**, 3450–3345.

50 S. Alwarappan, G. D. Liu and C. Z. Li, Simultaneous detection of dopamine, ascorbic acid, and uric acid at electrochemically pretreated carbon nanotube biosensors, *Nanomed. Nanotech. Biol. Med.*, 2010, **6**, 52–57.

51 L. Zhang, X. Geng, J. Zhou, Y. Wang, H. L. Gao, Y. Zhou and J. Huang, Fabrication of poly(γ-glutamic acid)-based biopolymer as the targeted drug delivery system with enhanced cytotoxicity to APN/CD13 over-expressed cells, *J. Drug Targeting*, 2015, **23**, 453–461.

52 W. J. Zhang, L. Liu, Y. G. Li, D. Y. Wang, H. Ma, H. L. Ren, Y. L. Shi, Y. J. Han and B. C. Ye, Electrochemical sensing platform based on the biomass-derived microporous carbons for simultaneous determination of ascorbic acid, dopamine, and uric acid, *Biosens. Bioelectron.*, 2018, **121**, 96–103.

53 Y. Yang, M. X. Li and Z. W. Zhu, A novel electrochemical sensor based on carbon nanotubes array for selective detection of dopamine or uric acid, *Talanta*, 2019, **201**, 295–300.

54 C.-X. Xu, K.-J. Huang, Y. Fan, Z.-W. Wu, J. Li and T. Gan, Simultaneous electrochemical determination of dopamine and tryptophan using a TiO$_2$-graphene/poly(4-aminobenzenesulfonic acid) composite film based platform, *Mater. Sci. Eng., C*, 2012, **32**, 969–974.

55 A. Abellán-Llobregat, L. Vidal, R. Rodríguez-Amaro;, A. Canals and E. Morallón, Evaluation of herringbone carbon nanotubes-modified electrodes for the simultaneous determination of ascorbic acid and uric acid, *Electrochim. Acta*, 2018, **285**, 284–291.

56 Q. Long, A. J. Fang, Y. Q. Wen, H. T. Li, Y. Y. Zhang and S. Z. Yao, Rapid and highly-sensitive uric acid sensing based on enzymatic catalysis-induced upconversion inner filter effect, *Biosens. Bioelectron.*, 2016, **86**, 109–114.

57 M. W. Khan, P. X. Zhao, A. Khan, F. Raza, S. M. Raza, M. Sarfraz, Y. Chen, M. Li, T. Yang, X. Ma and G. Y. Xiang, Synergism of cisplatin-oleanolic acid co-loaded calcium carbonate nanoparticles on hepatocellular carcinoma cells for enhanced apoptosis and reduced hepatotoxicity, *Int. J. Nanomed.*, 2019, **14**, 3753–3771.

58 S. Behera and C. Retna Raj, Mercaptoethylpyrazine promoted electrochemistry of redox protein and amperometric biosensing of uric acid, *Biosens. Bioelectron.*, 2007, **23**, 556–561.

59 Z. H. Wang, H. J. Guo, R. J. Gui, H. Jin, J. F. Xia and F. F. Zhang, Simultaneous and selective measurement of dopamine and uric acid using glassy carbon electrodes modified with a complex of gold nanoparticles and multiwall carbon nanotubes, *Sens. Actuators, B*, 2018, **255**, 2069–2077.

60 G. J. Zhang, B. Keita, R. N. Biboum, F. Miserque, P. Berthet, A. Dolbecq, P. Mialane, L. Catalae and L. Ndjo, Synthesis of various crystalline gold nanostructures in water: The polyoxometalate, ß-[H$_4$PMo$_{12}$O$_{40}$]$^{3-}$ as the reducing and stabilizing agent, *J. Mater. Chem.*, 2009, **19**, 8639–8644.

61 N. G. Tsierkezos, U. Ritter, Y. N. Thaha, C. Downing, P. Szroeder and P. Scharff, Multi-walled carbon nanotubes doped with boron as an electrode material for electrochemical studies on dopamine, uric acid, and ascorbic acid, *Microchim. Acta*, 2016, **183**, 35–47.

62 C. Pichon, P. Mialane, A. Dolbecq, J. Marrot, E. Rivière, B. Keita, L. Nadjo and F. Sécheresse, Characterization and electrochemical properties of molecular icosanuclear and bidimensional hexanuclear Cu(II) azido polyoxometalates, *Inorg. Chem.*, 2007, **46**, 5292–5301.

63 N. G. Tsierkezos, S. H. Othman, U. Ritter, L. Hafermann, A. Knauer, J. M. Köhler, C. Downing and E. K. McCarthy, Electrochemical analysis of ascorbic acid, dopamine, and uric acid on nobel metal modified nitrogen-doped carbon nanotubes, *Sens. Actuators, B*, 2016, **231**, 218–229.

64 A. Savk, B. Özdil, B. Demirkana, M. S. Nas, M. H. Calimli, M. H. Alma, Inamuddin, A. M. Asiri and F. Şen, Multiwalled carbon nanotube-based nanosensor for ultra-sensitive detection of uric acid, dopamine, and ascorbic acid, *Mater. Sci. Eng., C*, 2019, **99**, 248–254.

65 Y. K. Zhao, Z. Yang, W. X. Fan, Y. C. Wang, G. Z. Li, H. L. Cong and H. Yuan, Carbon nanotube/carbon fiber electrodes via chemical vapor deposition for simultaneous determination of ascorbic acid, dopamine and uric acid, *Arabian J. Chem.*, 2020, **13**, 3266–3275.

66 Y. F. Zhang, X. J. Bo, A. Nsabimana, A. Munyentwali, C. Han, M. Li and L. P. Guo, Green and facile synthesis of an Au nanoparticles@polyoxometalate/ordered mesoporous carbon tri-component nanocomposite and its electrochemical applications, *Biosens. Bioelectron.*, 2015, **66**, 191–197.